

## Clumpy Structures within the Turbulent Primordial Cloud

CHING-YAO TANG<sup>1,2</sup> AND KE-JUNG CHEN<sup>1</sup>

<sup>1</sup>*Institute of Astronomy and Astrophysics, Academia Sinica, Taipei 10617, Taiwan*

<sup>2</sup>*Department of Physics, National Taiwan University, Taipei 10617, Taiwan*

### ABSTRACT

This paper studies the effect of turbulence in the formation process of the Population III (Pop III) stars as known as the first stars, which play a key role in the cosmic evolution. Previous cosmological simulations of Pop III star formation suggested these stars would have a typical mass of  $\sim 100 M_{\odot}$ . However, this mass scale is inconsistent with the recent observations of the extremely metal-poor stars that infer the mass scale of the Pop III stars to be around  $25 M_{\odot}$ . This mass discrepancy may be due to the unresolved turbulence of the Pop III star-forming cloud driven by the accreting primordial gas during the mini-halo formation in the previous cosmological simulations. Unfortunately, such turbulent flow cannot be resolved in these simulations. To examine the effect of the turbulence in the Pop III star-forming cloud, we use the adaptive mesh refinement (AMR) code, *Enzo* to model the turbulent Pop III star-forming cloud using an artificial-driven turbulence scheme and including the relevant gas physics. This artificial-driven turbulence uses the stochastic forcing model to mimic the unresolved turbulence inside mini-halos. We find that several clumps with dense cores of  $22.7 - 174.9 M_{\odot}$  form in the turbulent Pop III star-forming cloud. These cores are subjected to the Jeans instability, and they will soon collapse to form stars. As turbulence becomes stronger and more compressive, the number of clumps increases. Our results suggest strong and compressive turbulence can effectively fragment primordial star-forming clouds and decrease the theoretical mass scale of Pop III stars that possibly resolves the mass discrepancy between simulations and observations.

*Keywords:* Cosmology, Turbulence, Hydrodynamics, Population III, Shortwaves, Early universe

### 1. INTRODUCTION

Based on the pioneering cosmological simulations, the first generation of stars (Population III stars in Greif & Bromm 2006, Population III.1 stars in O’Shea et al. 2008; hereafter Pop III stars) have brought the early universe out of the “cosmic dark ages” by emitting the first light to the dark cosmos at redshift  $z \sim 20 - 30$ , roughly 50 million years after the Big Bang (see Larson & Bromm 2001; Bromm et al. 2009; Bromm 2013; Greif 2015; Norman et al. 2018; Yoshida 2019, for reviews). Furthermore, the Pop III stars synthesize the first heavy elements (metals) through nuclear burning in their stellar interior; later the metals are dispersed to the intergalactic medium (IGM) through supernova explosion and chemically enrich the pristine gas for nurturing the next star formation (SF) (Bromm et al. 2003; Yoshida et al. 2004; Wise & Abel 2008; Greif et al. 2010; Bromm & Yoshida 2011; Chen et al. 2017b; Chiaki et al. 2018; Abe et al. 2021; Chen et al. 2022). The Pop III stars transform the simple early universe into the ever-increasingly complex status we observe today. Therefore, understanding how the Pop III stars formed from the primordial gas clouds is the key to understanding the genesis of our universe and life.

After the Big Bang, small matter perturbations seeded by the inflation start to grow through gravitational instabilities and eventually form into the gravitationally bound structures so-called “dark matter (DM) mini-halos” with a virial mass around  $10^5 - 10^6 M_{\odot}$  and a virial temperature of  $\sim 10^3$  K. Mini-halos amass the primordial gas and nurse the Pop III stars (Tegmark et al. 1997; Bromm et al. 2002; Yoshida et al. 2008). The primordial gas cloud is mainly made of H, He, and their derivatives (Tegmark et al. 1997; Yoshida et al. 2003, 2006) and likely contain tiny magnetic fields of  $< 10^{-10}$  gauss (Wagstaff et al. 2014; Jedamzik & Saveliev 2019; Sanati et al. 2020; McKee et al. 2020). Because

of the absence of dust and metal inside the mini-halos, molecular hydrogen becomes the major coolant that remains effective at temperature below  $10^4$  K (see Massimo Stiavelli 2009, chap.2), pre-determining a characteristic mass of the star-forming cloud. For a Pop III star-forming cloud, the mass fraction of  $\text{H}_2$  could reach  $\sim 10^{-4} - 10^{-3}$  with gas density  $n \sim 10^4 \text{ cm}^{-3}$ ; this condition allows the cloud to cool down to  $\sim 200$  K with a corresponding Jeans mass roughly equal to  $500 - 1000 M_\odot$ , and the cloud will undergo runaway collapse if its mass exceeds Jeans mass (Abel et al. 2002; Yoshida et al. 2003).

The direct observation of Pop III stars is far beyond the capability of our large telescopes; thus, the chemical abundance patterns from the observation of extremely metal-poor (EMP) stars, formed right after the first stars and their supernovae, have been used to probe the typical mass of Pop III stars via their supernova yields. The elemental abundance of the EMP stars implies that Pop III stars are of  $\sim 12 - 60 M_\odot$  (Umeda & Nomoto 2005; Ishigaki et al. 2018; Chen et al. 2017a). However, the cosmological zoom-in simulations of Pop III SF performed by Norman (2008); Hirano et al. (2014, 2015); Hosokawa et al. (2016) propose that the mass function of the Pop III stars is broadly distributed in  $\sim 50 - 1000 M_\odot$ . We suspect that this discrepancy between observation and simulation originates from the turbulent flow inside the mini-halo; previous simulations simply treat the star-forming gas inside the halos as subsonic, and they are unable to resolve the small-scale turbulence inside the Pop III forming cloud. Based on Tseliakhovich & Hirata (2010); Greif et al. (2011b), supersonic flow streams left over from the recombination epoch can produce strong turbulence inside the mini-halos and alter the gas structure of their star-forming clouds. Turbulence provides additional pressure support to prevent the cloud from the catastrophic collapse and possibly creates multiple high-density gas regions. Eventually, these dense regions are likely to form Pop III stars with stellar masses which probably explain the EMP observations.

For the above-mentioned reasons, we believe that properly modelling the subtle turbulent gas structures in the Pop III SF simulations should release the tension between simulation and observation. Due to the tremendous dynamical range from the IGM down to the star-forming cloud, resolving the whole energy cascading process of the turbulence in any cosmological simulations is impossible currently. To examine the effect of turbulence in Pop III SF, we use a stochastic forcing model to simulate the unresolved turbulence driven by the in-flowing gas during the mini-halo formation. By manipulating the properties of supersonic turbulence, we investigate the impact of turbulence on the gas dynamics inside the mini-halos and the consequent SF.

The structure of this paper is organized as follows. In Section 2, we first introduce the numerical methodology for simulating the turbulent Pop III star-forming cloud. We describe the evolution of the clouds in Section 3; then we present their physical properties in Section 4. In Section 5, we discuss the applications and limits of our simulations. Finally, we conclude our findings in Section 6.

## 2. NUMERICAL METHOD

### 2.1. Adaptive Mesh Refinement Code *Enzo*

We use the grid-based, adaptive mesh refinement (AMR) code *Enzo* (O’Shea et al. 2005; Bryan et al. 2014) to model the formation of primordial gas cloud with turbulence. The AMR technique (Berger & Colella 1989; Bryan 1999; Norman & Bryan 1999; Bryan & Norman 2000) automatically increase the spatial resolution if the designated physical quantities, such as density and velocity, of the grids satisfy the refinement criteria. *Enzo* combines the N-body scheme (Hockney & Eastwood 1988; Couchman 1991) for the collisionless particles and the Eulerian method for fluid dynamics; it solves the compressible Euler equations by means of MUSCL-based method (Wang et al. 2008) and second-order Runge-Kutta scheme (Shu & Osher 1988) for time integration. In this work, we use piecewise linear method (PLM; Van Leer 1979; Colella & Glaz 1985) and Harten-Lax-van Leer solver (HLL solver; Toro 2013) to solve the Riemann problem.

To modeling the Pop III SF cloud, we include the chemistry network of primordial gas involving nine main species: H,  $\text{H}^+$ ,  $\text{H}^-$ ,  $\text{H}_2$ ,  $\text{H}_2^+$ , He,  $\text{He}^+$ ,  $\text{He}^{++}$ , and  $e^-$  (Anninos et al. 1997; Abel et al. 1997, 2002; Ripamonti & Abel 2004; Turk et al. 2009). The gas cooling network considers collisional excitation and ionization, radiative recombination, free-free transition, etc., for atomic H and He; moreover, it includes the  $\text{H}_2$  cooling due to line, formation, and collision-induced emissions. The chemistry and cooling networks couple with the hydrodynamic equations self-consistently. Furthermore, the gas self-gravity is included by coupling the hydrodynamic equations with the gravitational potential calculated from the Poisson equation.

We utilize the stochastic forcing model developed by Schmidt et al. (2009). It generates the turbulence with a statistically isotropic stochastic force field, which accelerates the fluid on the large scales smoothly. This external force

field has been written as stochastic differential equation in Fourier  $\mathbf{k}$  space with a small spread of forcing wave numbers; then the solution in  $\mathbf{x}$  space is included as source terms in the momentum and energy equations of hydrodynamics. Besides, the nonlinear subgrid-scale (SGS) model from Grete et al. (2017) is used to deal with the unresolved scales of turbulence.

## 2.2. Simulation Setup

We perform the 3D *Enzo* simulations on a Cartesian coordinate grid:  $x$ ,  $y$ ,  $z$ , and the physical side length of the simulation box is 3 pc comparable to the size of central region of primordial clouds with masses:  $M_{gas}$  of  $3397 M_{\odot}$  and  $6041 M_{\odot}$ . The box is initially filled with the uniform primordial gas (76% H and 24% He by mass) of densities  $8.4 \times 10^{-21} \text{ g cm}^{-3}$  or  $1.5 \times 10^{-20} \text{ g cm}^{-3}$  and temperature 1000 K based on the previous cosmological simulations of Pop III star formation (Greif et al. 2011a; Hirano et al. 2015). The root grid has  $256^3$  cells with up to two levels of factor-two refinement ( $2^2$ ). The refinement criteria are based on the gas overdensity and Jeans length; the grid will be refined if gas density  $> 10^{-17} \text{ g cm}^{-3}$ , or the number of the cells covered one Jeans length is less than 16. The finest grids have a spatial resolution of  $\sim 604 \text{ AU}$ , which is roughly the size of proto-stellar envelope ( $\gtrsim 300 \text{ AU}$ ); therefore, the physical processes of dense core formation ( $n \sim 10^8 \text{ cm}^{-3}$ ) can be well resolved in our simulation.

### 2.2.1. Physical Scenario of Modelling the Turbulence in Primordial Gas

In our scenario, the primordial gas is accreted onto the halo center through the halo gravity during the assembly of DM mini-halos, and this process leads to the gravito-turbulence. The turbulence lasts until the turbulent primordial cloud becomes virialized. Then the cloud stops amassing the primordial gas, and the sub-halo turbulence commences diminishing. Meanwhile,  $\text{H}_2$  cooling dissipates the thermal energy injected from turbulence so that gas self-gravity becomes dominant. After that, the high-density gas clusters shaped by the turbulence can grow into gravitationally bound structures that will host the Pop III SF. To realize the above scenario, we divide our simulation into three different phases which will be described in the following sections.

### 2.2.2. Phase I: Stochastic Turbulence Development

Resolving the turbulence of Pop III star-forming region from the galactic scale down to protostellar object is still beyond the envelope of modern cosmological simulations. Since we are interested in the inner region of primordial cloud of several pc, we adopt the stochastic method with periodic boundary on all sides of the simulation box to model the innermost region of mini-halo instead of evolving the turbulence cascade from the scale larger than halo. We define this early stage of simulation as **Phase I**. The original algorithm of stochastic turbulence in *Enzo* only considers the isothermal gas. We modify this algorithm applicable for the ideal gas with the primordial chemistry and cooling network. In this phase, stochastic turbulence stirs up the primordial gas in an isotropic way, and the associated gas chemistry and cooling coevolve with the turbulence development. Stochastic force field will shape the gas structure inside the primordial cloud.

To explore the impact of turbulence on the primordial star-forming cloud, we select different combinations of two turbulence parameters in accordance with Schmidt et al. (2009) definition. First turbulence parameter is characteristic Mach number  $\mathcal{M}$ , where  $\mathcal{M} = V/c_0$ ,  $V$  is the characteristic velocity, and  $c_0$  is the initial sound speed. The second turbulence parameter is  $\mathcal{C}$  which represents the ratio between the compressional and solenoidal components in the force field. The turbulent flow becomes more compressive as  $\mathcal{C}$  increases. The model names and their parameters are summarized in Table 1.

### 2.2.3. Phase II: Turbulence Diminishing

Stochastic turbulence becomes dynamical equilibrium when the overall gas temperature reaches its minimum due to gas cooling. Then, we assume that turbulence starts to decay due to the halt of in-flowing gas and energy from the halo scale. Therefore, at this moment, we halve the characteristic Mach number every turnover time of the largest eddy  $\tau_{\text{eddy}} \sim l_{\text{eddy}}/v_{\text{rms}}$ , where  $l_{\text{eddy}}$  and  $v_{\text{rms}}$  are the largest eddy size (half of the box size) and the root mean square velocity of the gas. We repeat this reduction procedure until  $\mathcal{M}$  drops to 1. Meanwhile, a fixed potential of DM mini-halo is induced; the corresponding virial mass and radius are based on cosmological simulations from Greif et al. (2011a, 2012). The gravitational potential well of mini-halos follows the NFW profile (Navarro et al. 1996, 1997),

$$\rho_{\text{DM}}(r) = \frac{M_h}{4\pi \left(\frac{r_h}{c}\right)^3 \left[\ln(1+c) - \frac{c}{1+c}\right]} \frac{1}{r_s \left(1 + \frac{r}{r_s}\right)^2}, \quad (1)$$

Model	$\mathcal{M}$	$\mathcal{C}$	$M_{gas}$ [ $M_{\odot}$ ]	$\rho_i$ [ $\text{g cm}^{-3}$ ]	$M_h$ [ $M_{\odot}$ ]	$r_h$ [pc]
<i>M2C2S</i>	2	2	3397	$8.4 \times 10^{-21}$	$3 \times 10^5$	110
<i>M2C2D</i>			6041	$1.5 \times 10^{-20}$	$3.1 \times 10^5$	97
<i>M2C3S</i>		3	3397	$8.4 \times 10^{-21}$	$3 \times 10^5$	100
<i>M2C3D</i>			6041	$1.5 \times 10^{-20}$	$3.1 \times 10^5$	97
<i>M2C4S</i>		4	3397	$8.4 \times 10^{-21}$	$3 \times 10^5$	100
<i>M2C4D</i>			6041	$1.5 \times 10^{-20}$	$3.1 \times 10^5$	97
<i>M4C2S</i>	4	2	3397	$8.4 \times 10^{-21}$	$3 \times 10^5$	110
<i>M4C2D</i>			6041	$1.5 \times 10^{-20}$	$3.1 \times 10^5$	97
<i>M4C3S</i>		3	3397	$8.4 \times 10^{-21}$	$3 \times 10^5$	100
<i>M4C3D</i>			6041	$1.5 \times 10^{-20}$	$3.1 \times 10^5$	97
<i>M4C4S</i>		4	3397	$8.4 \times 10^{-21}$	$3 \times 10^5$	100
<i>M4C4D</i>			6041	$1.5 \times 10^{-20}$	$3.1 \times 10^5$	97
<i>M8C2S</i>	8	2	3397	$8.4 \times 10^{-21}$	$3 \times 10^5$	110
<i>M8C2D</i>			6041	$1.5 \times 10^{-20}$	$3.1 \times 10^5$	97
<i>M8C3S</i>		3	3397	$8.4 \times 10^{-21}$	$3 \times 10^5$	100
<i>M8C3D</i>			6041	$1.5 \times 10^{-20}$	$3.1 \times 10^5$	97
<i>M8C4S</i>		4	3397	$8.4 \times 10^{-21}$	$3 \times 10^5$	100
<i>M8C4D</i>			6041	$1.5 \times 10^{-20}$	$3.1 \times 10^5$	97

**Table 1.** Model parameters. From left to right: model name, characteristic Mach number  $\mathcal{M}$ , ratio between the compressional and solenoidal components  $\mathcal{C}$ , total gas mass  $M_{gas}$  in the simulation box, initial gas density  $\rho_i$ , corresponding virial mass  $M_h$  and virial radius  $r_h$  of the mini-halo in accordance with Greif et al. (2011a, 2012).

where  $M_h$  and  $r_h$  are virial mass and virial radius of the halo,  $r_s$  is the scale radius, and  $c = r_h/r_s$  is the concentration parameter, which is 20 in this study. Halo potential is placed at the box center. The halo gravity amass the the turbulent gas into the halo center. The evolution of turbulence reduction with a halo gravity described above is named as **Phase II**.

#### 2.2.4. Phase III: Dense Core Formation

We decrease the strength of driven turbulence until the dense gas is reaching a slowly collapsing state based on the virialization parameter, defined in (Wise et al. 2008),

$$\beta = \frac{3(\gamma - 1)E_{th} + 2E_k}{E_s - U} - 1, \quad (2)$$

where  $E_{th}$ ,  $E_k$ ,  $E_s$ , and  $U$  denote the thermal energy, kinetic energy, surface pressure work, and the gravitational potential energy, respectively.  $\gamma$  is the adiabatic index, which we adopt 5/3 for the ideal monatomic gas in the  $\beta$  calculation. Because we aim to evaluate the virialization status of the gas system, both the gravitational binding energy within the gas  $U_b$  and DM potential energy  $U_{DM}$  acting on the gas are included in term  $U$ . When  $\beta$  drops to zero, we shut down the stochastic force field and turn on the gas self-gravity, which becomes predominant force in the weakened turbulence and further grows the clumpy structures in the cloud. Besides, the boundary condition is changed from the periodic to outflow for simulating the collapsing cloud. We can call this final phase of simulation as **Phase III**.

During the **Phase III** simulation, the high-density gas clusters grow in mass and become gravitationally bound. If the maximum gas density in the simulation exceeds  $10^{-15} \text{ g cm}^{-3}$ , the three-body reaction will rapidly convert most of the hydrogen atom into molecular form (Turk et al. 2010). Fully molecular gas can cool and condense rapidly; however, due to the limits of spacial resolution and missing small-scale microphysics, we fail to evolve our simulations further. Thus, we have to terminate the simulations when the maximum density reaches  $\sim 10^{-16} \text{ g cm}^{-3}$ . Finally, we summarize the procedure of simulation including three major phases in Figure 1.

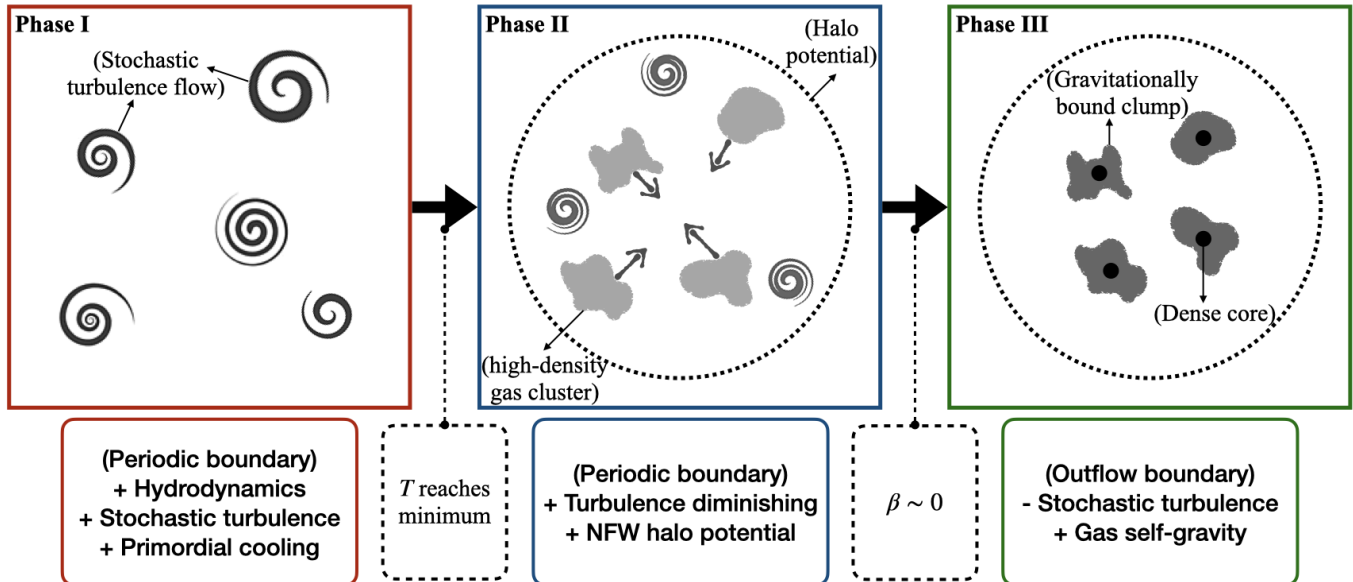
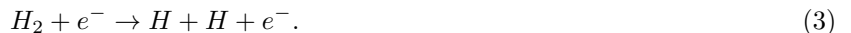


**Figure 1.** Flowchart of simulating the turbulent primordial cloud in our model. We separate the simulation into three phases, and the physical processes included or excluded in each phase are shown in the text box below the cartoon. The transition point between two consecutive phases is according to the criterion stated in the dashed-line text box.

### 3. EVOLUTION OF THE TURBULENT PRIMORDIAL CLOUD

#### 3.1. Chemical and Thermal Evolution

We first demonstrate the time evolution of the  $H_2$  mass fraction (hereafter  $H_2$  fraction) and mass-weighted temperature in **Phase I** in the left panel of Figure 2. As shown in the figure,  $H_2$  fraction rapidly increases from zero to  $\sim 10^{-4}$  within the first 0.03 – 0.5 million years after the simulation begins; then, the molecular hydrogen cooling effect becomes substantial. For models with the same  $\mathcal{M}$ , they have similar growing tracks of  $H_2$  fraction. In general, the higher  $\mathcal{M}$  models can produce more  $H_2$  fraction since they generate highly compressed flow and create denser gas regions which favor  $H_2$  fraction formation. For the fixed  $\mathcal{M}$  models with different  $\mathcal{C}$ , the deviation among evolutionary tracks becomes more significant as  $\mathcal{M}$  increases. Our results suggest that  $H_2$  formation is more sensitive to  $\mathcal{M}$  than  $\mathcal{C}$ . However, unlike the growing evolutionary tracks in  $\mathcal{M} = 2$  and 4, those in  $\mathcal{M} = 8$  fluctuate at the late time due to the collisional dissociation of  $H_2$  by free electrons (Abel et al. 1997),



While the stochastic turbulence evolves, the driven eddies inject kinetic energy into the primordial clouds. Then part of gas kinetic energy converts to the thermal energy by compressing the fluid; subsequently, it leads to the increment of gas density, temperature, and  $H_2$ . As shown in the right panel of Figure 2, temperatures increase from 1000 to 2200 – 5400 K within the first 0.03 – 0.3 million years after the simulation begins. After the gas temperatures reach their peaks, they start to drop due to the enhanced  $H_2$  cooling and finally cool down to an equilibrium ( $\lesssim 400$  K in  $\mathcal{M} = 2$  and 4 models). Similar to the  $H_2$  fraction evolutionary tracks, the temperature tracks in the fixed  $\mathcal{M}$  models are similar. However, temperatures in  $\mathcal{M} = 8$  models vary largely at the late time and remain  $\sim 1000 - 2000$  K, which is higher than the equilibrium temperatures of other  $\mathcal{M}$  models. Because strong turbulence in  $\mathcal{M} = 8$  models keeps pumping energy into the cloud over the amount that it can dissipate. Despite the temperature fluctuation in  $\mathcal{M} = 8$  models, we select the snapshot of roughly 1000 K as the starting point of the **Phase II** simulation.

Figure 3 shows the gas mass distribution as a function of Mach number at the end of the **Phase I** simulation. Since our turbulence system is non-isothermal, the gas temperature in the simulation domain can range from 10 to  $10^5$  K and causes the Mach numbers of the gas flow spread from 0.1 (subsonic) to several hundreds (hypersonic). Nevertheless, the Mach number of  $> 95\%$  gas in each model remains close to the characteristic  $\mathcal{M}$  we assign. The gas with extremely high and low Mach numbers is  $< 1\%$  by mass.

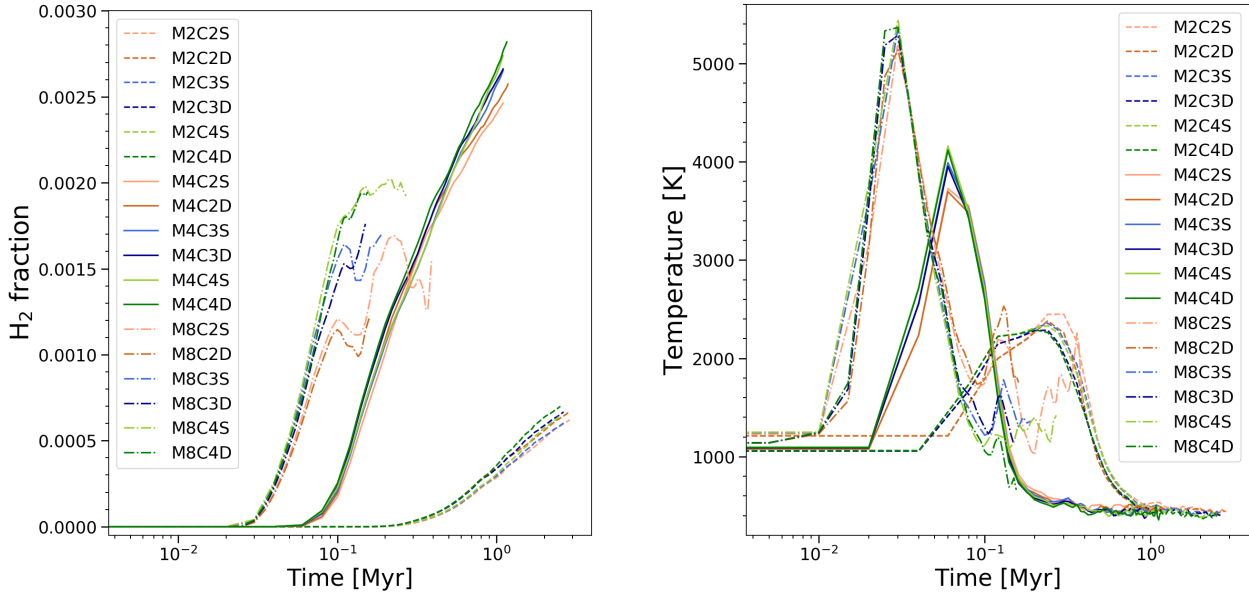


**Figure 2.** Evolution of overall  $\text{H}_2$  mass fraction (left panel) and mass-weighted temperature (right panel) in the **Phase I** simulation. The evolutionary tracks group with  $\mathcal{M}$  in both  $\text{H}_2$  fraction and temperature;  $\mathcal{C}$  is a minor factor to the overall chemi-thermal evolution. Large fluctuations occur in  $\mathcal{M} = 8$  models because of the  $\text{H}_2$  dissociation.

### 3.2. Virialization of the Cloud

We show the evolution of virialization parameter of **Phase II** simulation in Figure 4. Overall,  $\beta$  declines as we gradually reduce the strength of the stochastic forcing field. In the beginning of this phase, higher  $\mathcal{M}$  models have larger  $\beta$  because of a stronger driving force and energy injection. After  $\text{H}_2$  forms in the high-density region shaped by the turbulence, part of turbulence then starts to dissipate through  $\text{H}_2$  cooling, and the  $\beta$  drops to zero except for the models with high  $\mathcal{M}$  but low  $\mathcal{C}$ . Higher  $\mathcal{M}$  cloud has more energy injection but a less efficient  $\text{H}_2$  cooling as we discussed in Section 3, and tends to be against global collapse. The less compressive turbulence in lower  $\mathcal{C}$  models form a relatively sparse gas configuration. As the result, strong turbulence is responsible for the larger  $E_k$  and  $E_{th}$  in  $\beta$ , and weak compression causes a smaller  $|U_b|$  and inefficient  $\text{H}_2$  cooling. Therefore,  $\beta$  in these models fails to drop below 0.

To visualize the gas structure evolution, we show the spatial distributions of projection gas density (column density) in Figure 5. At the end of the **Phase I** simulation (column 1 in the figure), turbulent flow is developed in a relatively isotropic configuration due to the nature of the stochastic forcing field. After the decay of turbulence and the gravitational pull of DM halo potential in **Phase II** (column 2), gas flow starts to concentrate around the central region. Meanwhile, clumpy structures form in the turbulent clouds. Eventually, some compact regions become Jeans unstable and further collapse into high-density objects in the **Phase III** as shown in the third column.

## 4. CLUMPY STRUCTURES IN THE TURBULENCE

In the following sections, we analyze the physical parameters of the turbulent Pop III primordial clouds to investigate the criteria for forming the dense clumpy structures, the candidates of the Pop III star-forming sites. Then we study the physical properties of the gravitationally bound clumps formed in the simulations by illuminating the chemi-thermal composition and the developing history of the clumps. Finally, we define dense cores from collapsing clumps and discuss their possible outcomes of SF.

### 4.1. Turbulence Effect

To examine the effect of turbulence properties on the gas structure, we first compare the projection density plots between different models in Figure 5. In **Phase I** (column 1 in the figure), the gas configurations seem similar; whereas higher  $\mathcal{C}$  clouds are more structured by showing more relatively low-density areas (blue areas in the plots). After turbulence diminishes (column 2), only the dense regions in  $\mathcal{C} = 4$  clouds grow in density (row b and d); on the other hand, in  $\mathcal{C} = 2$  models, preceding high-density objects become diffusive as the turbulence strength decreases.

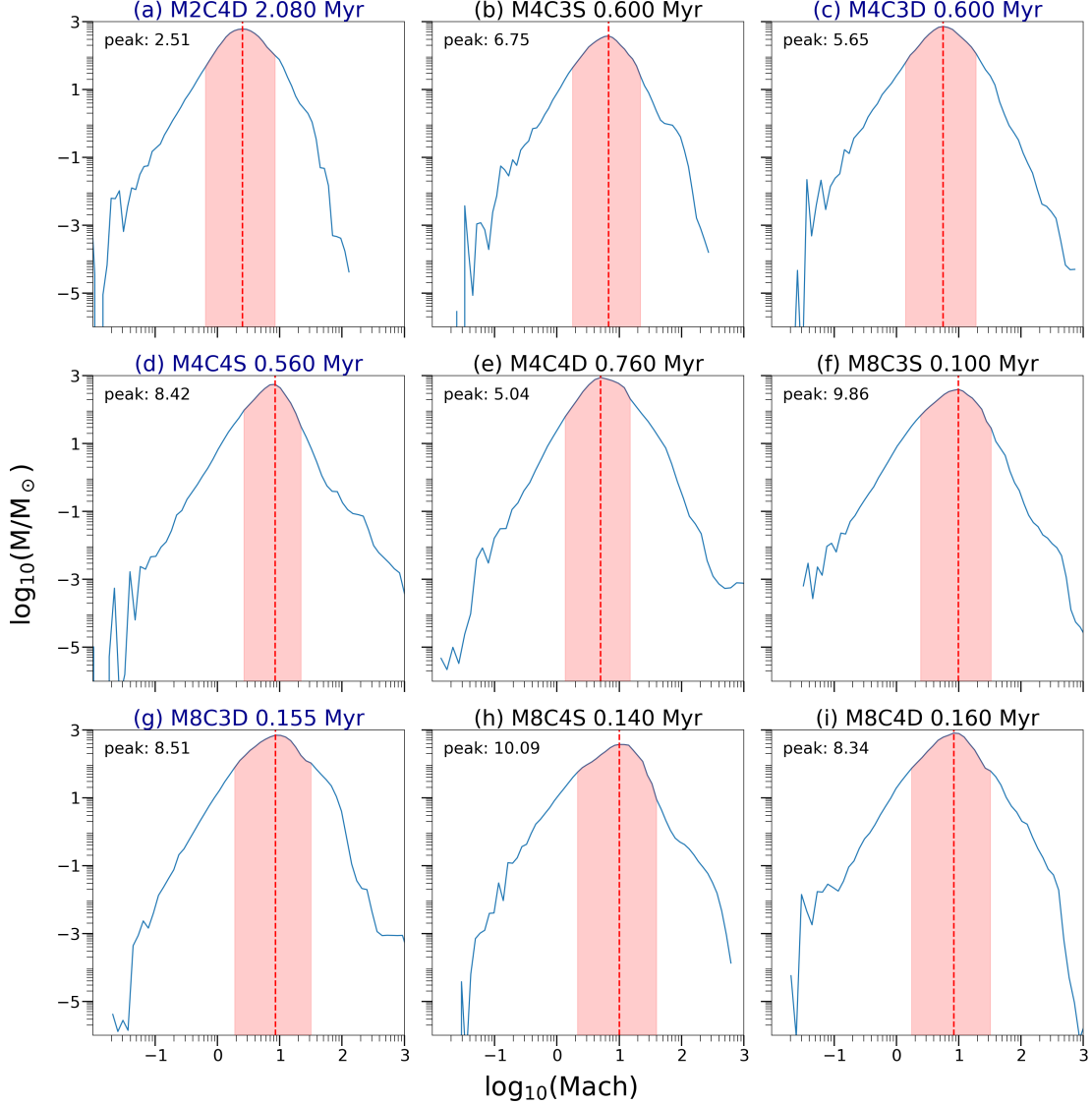


**Figure 3.** Gas mass distribution as a function of Mach number at the end of the **Phase I** simulation. The location of the peak indicated by the red-dashed line shows the Mach number bin containing the most mass, and its value is marked on the upper left corner in each panel. Besides, the red-shaded area covers 95% of the gas mass around the peak. At this moment, the peak Mach number roughly corresponds to  $\mathcal{M}$  of the model. The models with panel titles in dark blue color do not form gravitationally bound structure in **Phase III**.

Several local gas clusters with relatively high density have been formed exclusively in high  $\mathcal{M}$  and  $\mathcal{C}$  models such as *M8C4D*. In **Phase III** (column 3), self-gravity of gas is the dominating force in the evolution of gas clusters, and it further solidifies these high-density structures in  $\mathcal{C} = 4$ . However, the high-density gas clusters can hardly form in  $\mathcal{C} = 2$  (row a and c).

We present the density projection for models which have formed gravitationally bound clumps (GBCs or clumps in short) at the end of the entire simulation in Figure 6. Each GBC consists of at least one dense core (star mark in the figure), which will be discussed in Section 4.3. For three  $\mathcal{M} = 4$  models, two of them form a single clump in the gas cloud; in contrast, three  $\mathcal{M} = 8$  models create 2–4 clumps. Besides, extensive fragmentary structure is found in high  $\mathcal{M}$  cases. An unique clump in *M8C4S* contains two dense cores, and it implies that clump fragmentation can occur in strong turbulence ( $\mathcal{M} \geq 8$ ). We show the correlation between the number of GBCs and the turbulence properties in the left panel of Figure 7. Our results suggest that the number of GBCs positively correlates with the  $\mathcal{M}$  and  $\mathcal{C}$  of

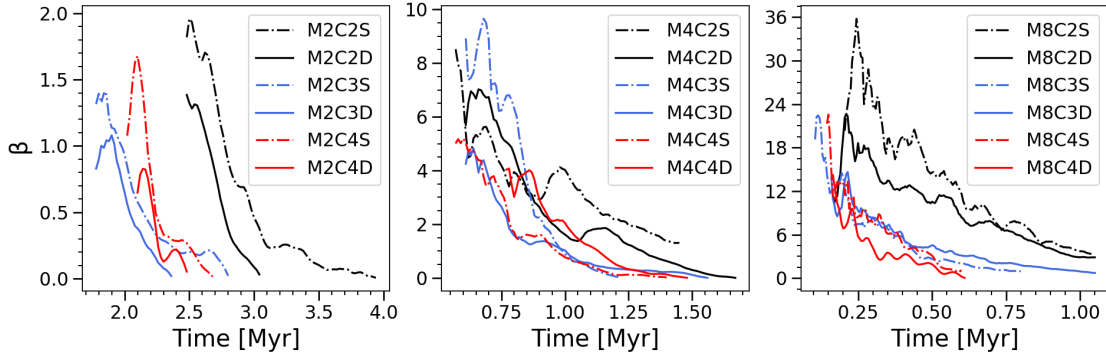


**Figure 4.** Evolution of virialization parameter  $\beta$  during the **Phase II** simulation. Three panels correspond to  $\mathcal{M} = 2, 4$ , and  $8$ , respectively.  $\beta$  declines as time because we gradually reduce the turbulence strength, and the turbulence energy has been released by cooling. Except for three  $\mathcal{C} = 2$  models,  $\beta$  drops to about zero at the end of **Phase II**.

turbulence. Moreover, no GBC can form in weak ( $\mathcal{M} \leq 2$ ) or low compressional ( $\mathcal{C} \leq 2$ ) turbulence. In other words, strong and highly compressive turbulence likely reshapes a single cloud into clumps of smaller masses.

The evolution of the maximum gas density in the **Phase III** simulations is shown in the right panel of Figure 7. Overall, only models with  $\mathcal{M} \geq 4$  and  $\mathcal{C} \geq 3$  can fulfill the density threshold and form GBCs. However, high  $\mathcal{M}$  and  $\mathcal{C}$  are the necessary but insufficient conditions to the GBC formation. Once gas self-gravity is activated in this phase, maximum densities in models contained GBCs increase rapidly due to the collapse of densest structure in GBCs. The densest regions in *M8C4S* and *M8C4D* have become Jeans unstable and collapse momentarily. Turbulence in these models has compressed part of the cloud into an over-dense state predominated by self-gravity. For *M8C3S*, *M4C4D*, and *M4C3S*, clumps continue growing in mass and follow the collapse of their dense cores.

Previously, we have mentioned that  $\mathcal{M} \geq 4$  and  $\mathcal{C} \geq 3$  are the necessary but insufficient conditions to form GBCs. Our results imply that only the models with strong and highly compressive turbulence ( $\mathcal{M} = 8$  and  $\mathcal{C} = 4$ ) can seed clumps in both mass scales (*M8C4S* and *M8C4D*). On the other hand, three models—*M8C3D*, *M4C4S*, and *M4C3D*—fail to form GBCs, but their either low or high mass counterpart models (*M8C3S*, *M4C4D*, and *M4C3S*) do. Therefore, the GBC formation is insensitive to the overall cloud mass. In Figure 8, we follow the evolution of *M8C3D* and *M4C3D*. No significant gas accretion occurs in the **Phase II** (panel a1 and a2) in *M4C3D*. Although part of gas does assemble at the boundaries of the simulation box after the self-gravity activate, these gas clusters are not massive enough to reach Jeans unstable and forge SF. In model *M8C3D*, high-density gas clusters (upper left corner of panel b1) have formed at the early stage; however, they are destroyed later by stochastic turbulence. Other high-density gas clusters form in lower right corner in panel b2, but they fail to evolve into gravitationally bound structures till the end. In summary, turbulence has both positive and negative impacts on GBC formation due to its nature of randomness; in weaker and lower compressional turbulence ( $\mathcal{M} \leq 4$  and  $\mathcal{C} \leq 3$ ), the destruction effect could become stronger than the compression effect and inhibit the GBC formation.

#### 4.2. Clumps' Properties

We show the temperature-density- $\text{H}_2$  phase diagram of the clumps in Figure 9. In general, the distribution of similar molecular hydrogen fractions in the diagram has a diagonal trend from lower-left to upper-right. Since the cooling rate is proportional to  $\text{H}_2$  fraction, mass contraction leads to temperature and density growth under the same cooling efficiency. That the gas with higher  $\text{H}_2$  fraction distributes across the lower right corner implies that denser gas can cool down the temperature due to more efficient cooling. The clumps in stronger and higher compressional turbulence have a greater overall  $\text{H}_2$  fraction, which agrees with the result of the entire gas system we discussed in Section 3.1. Besides, the clumps in models of  $\mathcal{M} = 8$  can even cool to below 100 K. Although these six clumps shown in Figure 9 contain the densest objects in their simulations, the variation of molecular hydrogen fraction is smaller than a factor of two despite two times difference in  $\mathcal{M}$ . A similar comparison to  $\mathcal{M} = 4$  and 2 models, their molecular hydrogen fractions deviate roughly a factor of ten. The bottleneck of the molecular hydrogen fraction growth suggests that turbulence has reached its limitation in catalyzing  $\text{H}_2$  formation. Gas self-gravity is required to further condense the clump and trigger the rapid three-body reaction of hydrogen. However, such a high density region is beyond the capability of our simulation, we thus stop the simulation when the maximum density of clumps exceeds  $\sim 10^{-16} \text{ g/cm}^3$ .

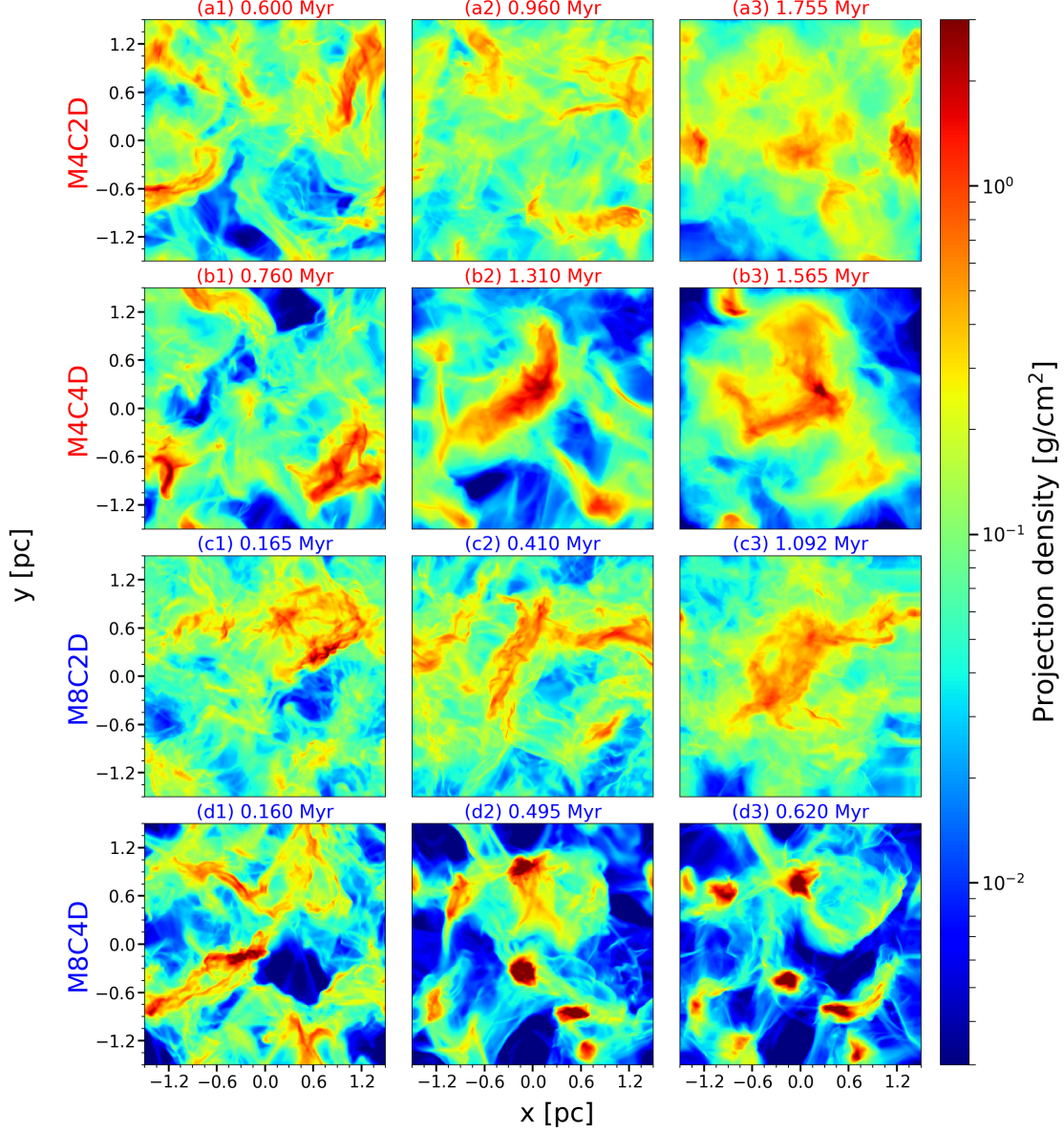


**Figure 5.** Evolution of gas projection density (column density) in the simulation. From left to right columns show the snapshots of gas column densities at **Phase I**, **Phase II**, and **Phase III**. Red and blue labels represent  $\mathcal{M} = 4$  and 8, correspondingly. Gas configurations evolve from a relatively isotropic distribution to a more concentrated structure through the simulation.  $\mathcal{C} = 4$  models form high-density gas cluster at the third phase; moreover, model  $M8C4D$  form multiple clusters caused by the turbulence fragmentation.

To investigate the physical properties of the GBCs, we approximate the clumps as a sphere centered at its maximum density and calculate their 1D radial profiles of density,  $\text{H}_2$  fraction, temperature, and in-fall rate at different evolution times in Figure 10. At the final snapshot ( $t_4$ , black lines), density and chemi-thermal configurations are similar among these clumps' inner region; all of them have a relatively hot and dense structure with little increment in  $\text{H}_2$  fraction. In  $\mathcal{M} = 4$ , the density and temperature change significantly from the **Phase II** to **Phase III** simulation; in contrast, clumps of  $\mathcal{M} = 8$  have a similar outer radial profile between the end of the **Phase II** and **Phase III** simulation ( $t_3$  and  $t_4$ ). It suggests that  $\mathcal{M} = 4$  turbulence fails to generate a clump scale ( $r \gtrsim 0.1$  pc) structure without gas self-gravity, but such structure can be shaped by a stronger turbulence ( $\mathcal{M} = 8$ ). Nevertheless, gas self-gravity is necessary to form a dense core of  $r \lesssim 0.05$  pc where the gravity dominates over gas pressure. The  $\text{H}_2$  fraction profile changes slightly over time, which means it has saturated under the turbulent flow without gas self-gravity.

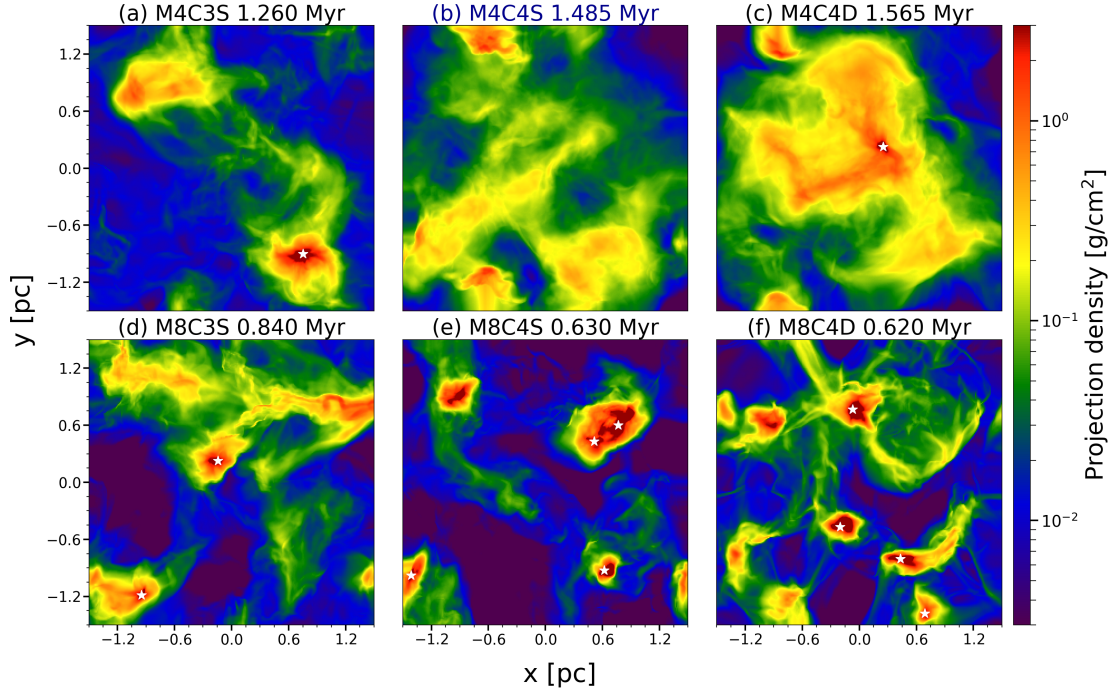


**Figure 6.** Density projection snapshots including all models that have formed GBC at the end of the entire simulation. White star mark indicates a local density maximum with the significant in-falling gas surrounding (regarded as core, which will be discussed in Section 4.2 and 4.3). In  $\mathcal{M} = 4$ , only single clump has formed in the simulation; in contrast,  $\mathcal{M} = 8$  models form 2 – 4 clumps. Plot (b) of *M4C4S* fails to form any clump at the end.

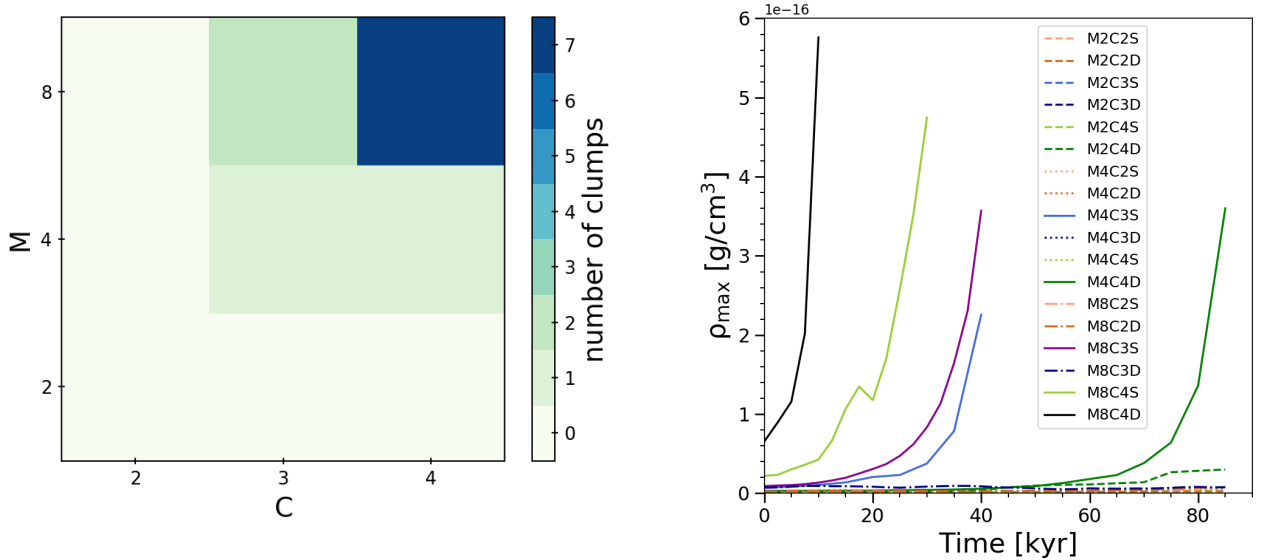


**Figure 7.** Left panel: The correlation among clump number,  $\mathcal{M}$ , and  $\mathcal{C}$ . Only the models with  $\mathcal{M} \geq 4$  and  $\mathcal{C} \geq 3$  form clumps. For  $\mathcal{M} = 8$ , clump number increases as  $\mathcal{C}$ . Right panel: Evolution of maximum gas density in the simulation during **Phase III**. The evolution time here starts from the beginning of **Phase III**. For the models that form GBCs, their maximum densities grow rapidly above the threshold we set for the simulation termination.

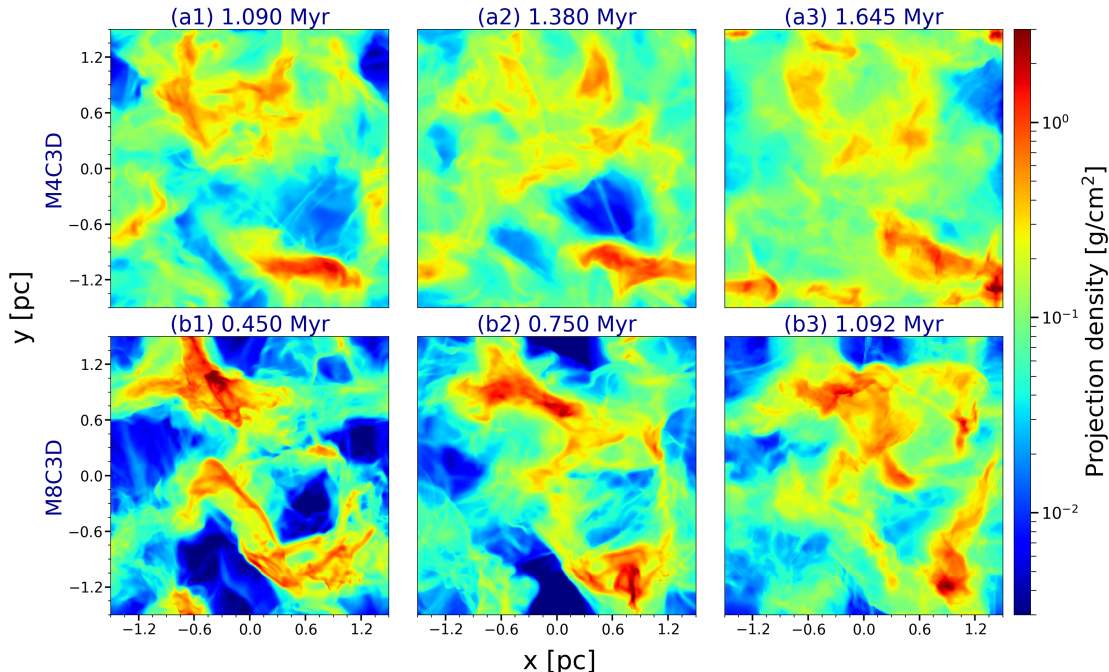


**Figure 8.** Density projection evolution of *M4C3D* and *M8C3D*. Three columns from left to right correspond to three time steps: The first column shows the snapshot after two turnover time when  $\mathcal{M}$  reduces to 1. The second and third columns show the snapshots of the end of **Phase II** and **Phase III** simulation. Although some high-density gas clusters form in **Phase II**, they still fail to grow into Jeans unstable objects.

Here, the in-fall rate  $R_{in-fall}$  of the clump is defined as

$$R_{in-fall}(r) = 4\pi r^2 \rho(r) v_{rad}(r), \quad (4)$$

where  $\rho$  is gas density, and  $v_{rad}$  is radial velocity toward the center. Similar to density and temperature structure, the prototype of the final configuration of  $R_{in-fall}$  has already emerged at the end of **Phase II** ( $t_3$ ) only in  $\mathcal{M} = 8$ . As a GBC is created at the end of the simulations, the in-fall rate has also appeared in the pattern increased with radius but saturated at the outer part, and this curve implies the collapsing clump. Inside the clump, that in-fall rate drops significantly indicates an accumulating object forms at the center. The radius of a dense core is defined as the radius where in-fall rate starts to decrease substantially in the clump.

#### 4.3. Dense Cores

Based on the in-fall rate curve at the end of the simulations, we identify the dense cores of GBCs and list their properties in Table 2; we discuss the possible stellar mass formed within these cores in Section 5.2. Among the cores with the densest center in each case, that the cores in higher  $\mathcal{M}$  and  $\mathcal{C}$  turbulence have higher maximum density means  $\rho_{max}$  depends on the turbulence compressibility. In our models, the core mass can range from 22.7 to 174.9  $M_\odot$ . Higher  $\mathcal{M}$  and  $\mathcal{C}$  turbulence generates more cores with various masses and naturally create both low and high mass cores due to different scales of convergent flows.

By assuming core as a rigid body, we can estimate the rotational velocity roughly 2 km s<sup>-1</sup>. For most of the cores, the ratio of the rotational velocity to its Kepler velocity  $f_{kep}$  is lower than 0.8 except *M8C4S-c*. Generally,  $f_{kep} < 1$  suggests the rotating structure can be bound by gravity. The core of *M8C4S-c* has  $f_{kep} = 1.844$  implying that the centrifugal force will break this core and create fragmentation.

## 5. DISCUSSIONS

### 5.1. Summary of the Turbulent Primordial Cloud Model

In the **Phase I** simulation, uniform primordial cloud is stirred by the stochastic forcing field. While turbulent structure gradually develops, the H<sub>2</sub> fraction grows to  $\sim 10^{-4}$ , and the gas temperature reaches a maximum value.

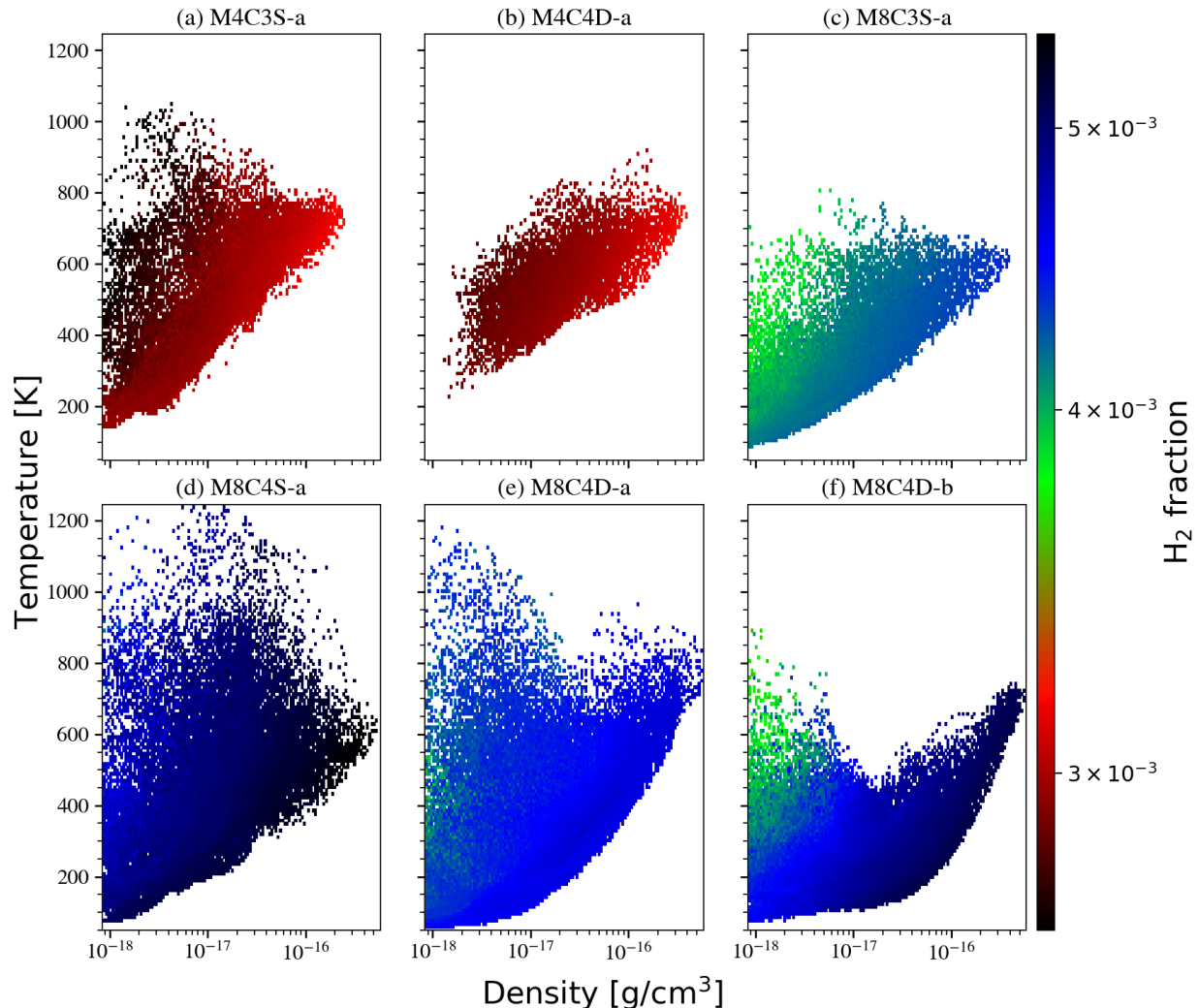


**Figure 9.** Density-temperature diagram with the associated  $\text{H}_2$  fraction of clumps at the end of the **Phase III** simulation. Each panel represent a GBC which a name and properties can be found in Table 2. In each clump, similar  $\text{H}_2$  fraction distributes in a diagonal trend from lower-left to upper-right. The high  $\text{H}_2$  fraction is distributed around higher density but lower temperature.

Then  $\text{H}_2$  fraction keeps increasing to  $\sim 10^{-3}$ , and the temperature attains a minimum equilibrium through molecular hydrogen cooling. Most of the gas have Mach number distributed around the corresponding  $\mathcal{M}$  of the model. When the turbulence becomes fully developed, we place a DM halo potential and weaken the driven force of turbulence as the simulation enters **Phase II**. Eventually, the virialization parameter of gas system drops to  $\sim 0$  at the end of **Phase II**. The gas distribution evolve from an isotropic configuration to a central-contracted structure due to the gravitational potential well of halo. After the stochastic turbulence is removed in the beginning of **Phase III**, the gas self-gravity becomes the dominating force in determining the gas dynamics on the scale  $< 0.1$  pc; the small-scale gas accretion due to the self-gravity not only collapses the existing GBCs to form dense cores at the center but also condenses the relatively less compact gas clusters to grow and generate dense cores as well.

Weak ( $\mathcal{M} \leq 2$ ) or less compressive ( $\mathcal{C} \leq 2$ ) turbulence cannot produce any GBCs after removing the external force field. Turbulence with  $\mathcal{M} \geq 4$  and  $\mathcal{C} \geq 3$  can form GBCs that further grow into dense cores at the end of simulations. However, intermediate turbulence with  $\mathcal{M} = 4$  or  $\mathcal{C} = 3$  generate either one clump or no clump due to the randomness nature of stochastic forcing turbulence. In the  $\mathcal{M} = 4$  models which have formed clumps, they create only a single dense core in the primordial cloud. Meanwhile,  $\mathcal{M} = 8$  can form multiple dense cores with various core mass; besides, the higher  $\mathcal{C}$  can increase the number of clumps.

## 5.2. From Dense Core to Stellar Mass

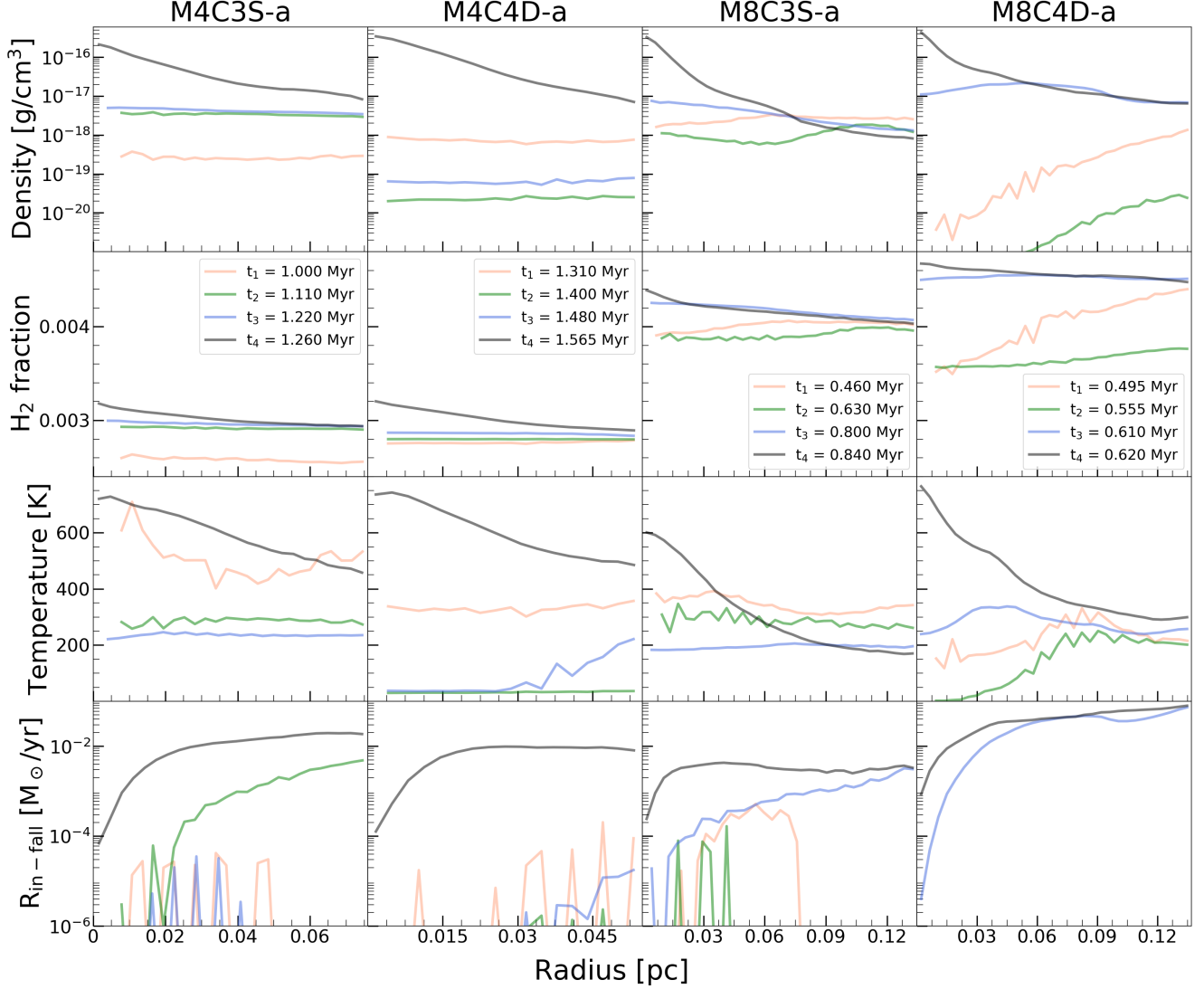


**Figure 10.** Clumps’ spherical-averaged profiles of density, H<sub>2</sub> mass fraction, temperature, and in-fall rate during **Phase II** and **Phase III**. We define four profile times as following:  $t_1$  is the snapshot after two turnover time when  $\mathcal{M}$  reduces to 1,  $t_2 = (t_1 + t_3)/2$ ,  $t_3$  is the end of the **Phase II** simulation, and  $t_4$  is the end of the **Phase III** simulation. The label of each clump can be found in Table 2. H<sub>2</sub> fraction only slightly increases over time. For the final density and temperature profiles, the centers of the clumps form into hot and dense structures, in which the in-fall rate drops substantially at  $r \lesssim 0.025$  pc.

The ultimate goal of our simulation is to find out the Pop III stellar mass. Under the limitation of our simulation, however, dense cores derived from the in-fall rate are the smallest high-density objects we can achieve. These cores can not be properly evolved further in our current simulations due to the lack of small-scale ( $\rho > 10^{-15}$  g cm<sup>-3</sup>) physics and finer spatial resolution. Instead, we infer the possible stellar mass by assuming the mass function of the stars resembles the core mass function (CMF) based on the result of [Guszejnov & Hopkins \(2015\)](#). Consequently, the profiles of CMF and initial mass function (IMF) are similar except a  $\sim 1/3$  shift of the peak value. Therefore, we divide the mass of cores by a factor of three to obtain their stellar mass range of  $8 - 59M_{\odot}$ . This mass range agrees with the typical Pop III stellar mass inferred from the EMP stars observation ([Ishigaki et al. 2018](#)).

On the other hand, different from the EMP star observation, [Chen et al. \(2022\)](#) suggests another method to probe the Pop III IMF through the first supernovae and galaxies, potentially observable targets to the James Webb Space Telescope (JWST). In sum, the forthcoming JWST observations of the early universe will shed light on the formation of Pop III stars.

Model	Core	$\rho_{max} [g \cdot cm^{-3}]$	$\mathbf{x}_{max} [pc]$	$r_{core} [pc]$	$M_{core} [M_{\odot}]$	$R_{in-fall} [M_{\odot} \cdot yr^{-1}]$	$L [g \cdot cm^2 \cdot s^{-1}]$	$f_{kep}$
<i>M4C3S</i>	a	$2.420 \times 10^{-16}$	(0.8,-0.9,-0.2)	0.027	80.7	$9.589 \times 10^{-3}$	$3.051 \times 10^{56}$	0.159
<i>M4C4D</i>	a	$3.773 \times 10^{-16}$	(0.3,0.2,-0.5)	0.018	52.1	$7.414 \times 10^{-3}$	$3.354 \times 10^{56}$	0.413
<i>M8C3S</i>	a	$3.841 \times 10^{-16}$	(-0.9,-1.2,-0.1)	0.019	46.1	$3.288 \times 10^{-3}$	$2.555 \times 10^{56}$	0.368
	b	$4.333 \times 10^{-17}$	(-0.1,0.2,-0.1)	0.048	94.5	$9.018 \times 10^{-4}$	$1.402 \times 10^{57}$	0.433
<i>M8C4S</i>	a	$5.077 \times 10^{-16}$	(0.8,0.6,-1.4)	0.035	112.2	$6.874 \times 10^{-3}$	$2.768 \times 10^{57}$	0.773
	b	$1.458 \times 10^{-16}$	(0.6,-0.9,-0.3)	0.027	48.7	$6.454 \times 10^{-4}$	$4.821 \times 10^{56}$	0.536
	c	$1.252 \times 10^{-16}$	(0.5,0.4,-1.2)	0.058	80.1	$5.565 \times 10^{-3}$	$5.126 \times 10^{57}$	1.844
	d	$7.347 \times 10^{-17}$	(-1.4,-1.0,0.9)	0.038	40.1	$7.180 \times 10^{-4}$	$1.835 \times 10^{56}$	0.230
<i>M8C4D</i>	a	$5.862 \times 10^{-16}$	(-0.2,-0.5,0.8)	0.036	174.9	$2.963 \times 10^{-2}$	$2.226 \times 10^{57}$	0.315
	b	$5.836 \times 10^{-16}$	(0.4,-0.8,-0.2)	0.022	102.1	$2.391 \times 10^{-2}$	$9.523 \times 10^{56}$	0.387
	c	$5.717 \times 10^{-17}$	(-0.1,0.8,-0.4)	0.036	46.6	$4.432 \times 10^{-3}$	$6.448 \times 10^{56}$	0.663
	d	$2.082 \times 10^{-17}$	(0.7,-1.4,1.0)	0.032	22.7	$9.108 \times 10^{-4}$	$1.144 \times 10^{56}$	0.368

**Table 2.** Properties of the dense cores. From left to right: model name, core label, maximum density inside the core  $\rho_{max}$ , position of the maximum density  $\mathbf{x}_{max}$ , core radius  $r_{core}$ , gas mass within core radius  $M_{core}$ , in-fall rate at core radius  $R_{in-fall}$ , core's total angular momentum  $L$ , ratio of rotation to Keplerian velocity  $f_{kep}$ .

### 5.3. Formation of Very Massive Pop III stars

In our  $\mathcal{M} = 2$  or low  $\mathcal{C} = 2$  models, they can not produce adequate high-density regions on the small scale, but the turbulent motion prevents the direct collapse of the cloud. Accordingly, weak or low compressional turbulence fail to form dense cores during the development process. After the cooling mechanism releases turbulence energy, the primordial cloud may undergo a large-scale collapse similar to the previous cosmological simulations, resulting in much massive Pop III stars over  $100M_{\odot}$ . Therefore, our model can naturally produce a wide mass scale to bridge the low-mass and high-mass end of Pop III stars.

### 5.4. Further Improvement for the Current Model

So far we have examined the impact of turbulence on the primordial cloud through an artificial driven turbulence. However, the turbulence structure is not self-consistently generated. Therefor, simulating a gravitational-driven turbulence during mini-halos formation may probe the nature of turbulence in the Pop III SF cloud.

Our simulation stops at  $\rho_{max} \sim 10^{-16} g \cdot cm^{-3}$  since we have not included all the relevant small-scale physics and finer spatial resolution. If the simulation attempts to evolve the dense core to a fully molecular core formed via rapid three-body reaction, the equation of state for high-density molecular gas should be included. Besides, the magnetic field is needed to transfer the angular momentum of the proto-stellar disk, allowing a proto-star to accrete gas successively. After including all these physics, our simulation can adopt a higher resolution to evolve the cores and the consequent SF.

## 6. CONCLUSION

Our study provides a possible solution for the discrepancy of Pop III stellar mass between the EMP star observation and the Pop III simulation. In the cosmological zoom-in simulation, extremely massive Pop III stars form via a runaway core collapse scenario of the primordial cloud, which may be suppressed if the sub-halo turbulence is resolved. We present a stochastic method to reproduce the turbulent structure inside the primordial cloud and investigate how turbulence affects the gas configuration and the potential star-forming site.

The results show that only adequately strong ( $\mathcal{M} \geq 4$ ) and highly compressive ( $\mathcal{C} \geq 3$ ) turbulence can generate locally fragmentary structures ( $\gtrsim 0.1$  pc) in the primordial cloud. Besides, turbulence with stronger compressibility (higher  $\mathcal{M}$  and  $\mathcal{C}$ ) forms more gas clumps that are gravitationally bound. Finally, these clumps result in dense cores with mass range from  $22.7 M_{\odot}$  to  $174.9 M_{\odot}$  at the end of our simulations. Based on the relation between CMF and IMF discovered by [Guszejnov & Hopkins \(2015\)](#), we infer the final Pop III stellar mass range of these dense cores is roughly  $\sim 8 - 59 M_{\odot}$ , which agrees with the EMP star observation.

For the  $\mathcal{M} = 2$  or  $\mathcal{C} = 2$  turbulence, the scenario is similar to the monolithic collapse of primordial gas in the mini-halo suggested by the previous cosmological simulations. Therefore, our turbulent primordial gas model can bridge between the low and high mass Pop III stars. In future work, we will improve our model with more realistic initial conditions and finer physics and resolution to probe the characteristic mass and IMF of Pop III stars. With the JWST observation and sophisticated models, we will soon peak into the cosmic dawn through understanding the birth of the first stars.

#### Acknowledgement

This research is supported by the National Science and Technology Council under grant no. MOST 110-2112-M-001-068-MY3 and the Academia Sinica, Taiwan under a career development award under grant no. AS-CDA-111-M04. Our computing resources were supported by the National Energy Research Scientific Computing Center (NERSC), a U.S. Department of Energy Office of Science User Facility operated under Contract No. DE-AC02-05CH11231, and the TIARA Cluster at the Academia Sinica Institute of Astronomy and Astrophysics (ASIAA).

#### REFERENCES

- Abe, M., Yajima, H., Khochfar, S., Dalla Vecchia, C., & Omukai, K. 2021, *MNRAS*, 508, 3226
- Abel, T., Anninos, P., Zhang, Y., & Norman, M. L. 1997, *New Astronomy*, 2, 181
- Abel, T., Bryan, G. L., & Norman, M. L. 2002, *science*, 295, 93
- Anninos, P., Zhang, Y., Abel, T., & Norman, M. L. 1997, *New Astronomy*, 2, 209
- Berger, M. J., & Colella, P. 1989, *Journal of computational Physics*, 82, 64
- Bromm, V. 2013, *Reports on Progress in Physics*, 76, 112901
- Bromm, V., Coppi, P. S., & Larson, R. B. 2002, *The Astrophysical Journal*, 564, 23
- Bromm, V., & Yoshida, N. 2011, *ARA&A*, 49, 373
- Bromm, V., Yoshida, N., & Hernquist, L. 2003, *The Astrophysical Journal*, 596, L135
- Bromm, V., Yoshida, N., Hernquist, L., & McKee, C. F. 2009, *Nature*, 459, 49
- Bryan, G. L. 1999, *Computing in Science & Engineering*, 1, 46
- Bryan, G. L., & Norman, M. L. 2000, in *Structured Adaptive Mesh Refinement (SAMR) Grid Methods* (Springer), 165–170
- Bryan, G. L., Norman, M. L., O’Shea, B. W., et al. 2014, *The Astrophysical Journal Supplement Series*, 211, 19
- Chen, K.-J., Heger, A., Whalen, D. J., et al. 2017a, *MNRAS*, 467, 4731
- Chen, K.-J., Tang, C.-Y., Ho, M.-Y., et al. 2022, arXiv preprint arXiv:2211.06016
- Chen, K.-J., Whalen, D. J., Wollenberg, K. M. J., Glover, S. C. O., & Klessen, R. S. 2017b, *ApJ*, 844, 111
- Chiaki, G., Susa, H., & Hirano, S. 2018, *MNRAS*, 475, 4378
- Colella, P., & Glaz, H. M. 1985, *Journal of Computational Physics*, 59, 264
- Couchman, H. 1991, *The Astrophysical Journal*, 368, L23
- Greif, T. H. 2015, *Computational Astrophysics and Cosmology*, 2, 1
- Greif, T. H., & Bromm, V. 2006, *Monthly Notices of the Royal Astronomical Society*, 373, 128
- Greif, T. H., Bromm, V., Clark, P. C., et al. 2012, *Monthly Notices of the Royal Astronomical Society*, 424, 399
- Greif, T. H., Glover, S. C., Bromm, V., & Klessen, R. S. 2010, *The Astrophysical Journal*, 716, 510
- Greif, T. H., Springel, V., White, S. D., et al. 2011a, *The Astrophysical Journal*, 737, 75
- Greif, T. H., White, S. D., Klessen, R. S., & Springel, V. 2011b, *The Astrophysical Journal*, 736, 147
- Grete, P., Vlaykov, D. G., Schmidt, W., & Schleicher, D. R. 2017, *Physical Review E*, 95, 033206
- Guszejnov, D., & Hopkins, P. F. 2015, *Monthly Notices of the Royal Astronomical Society*, 450, 4137
- Hirano, S., Hosokawa, T., Yoshida, N., Omukai, K., & Yorke, H. W. 2015, *Monthly Notices of the Royal Astronomical Society*, 448, 568
- Hirano, S., Hosokawa, T., Yoshida, N., et al. 2014, *The Astrophysical Journal*, 781, 60
- Hockney, R. W., & Eastwood, J. W. 1988, *Computer simulation using particles* (crc Press)
- Hosokawa, T., Hirano, S., Kuiper, R., et al. 2016, *The Astrophysical Journal*, 824, 119
- Ishigaki, M. N., Tominaga, N., Kobayashi, C., & Nomoto, K. 2018, *The Astrophysical Journal*, 857, 46
- Jedamzik, K., & Saveliev, A. 2019, *Physical review letters*, 123, 021301
- Larson, R. B., & Bromm, V. 2001, *Scientific American*, 285, 64

- Massimo Stiavelli. 2009, *From First Light to Reionization* (Wiley-VCH)
- McKee, C. F., Stacy, A., & Li, P. S. 2020, *Monthly Notices of the Royal Astronomical Society*, 496, 5528
- Navarro, J. F., Frenk, C. S., & White, S. D. 1997, *The Astrophysical Journal*, 490, 493
- Navarro, J. F., Frenk, C. S., & White, S. D. M. 1996, *The Astrophysical Journal*, 462, 563
- Norman, M. L. 2008, in *AIP Conference Proceedings*, Vol. 990, American Institute of Physics, 3–15
- Norman, M. L., & Bryan, G. L. 1999, in *Numerical Astrophysics* (Springer), 19–28
- Norman, M. L., Smith, B. D., & Bordner, J. 2018, *Frontiers in Astronomy and Space Sciences*, 34
- O’Shea, B. W., McKee, C. F., Heger, A., & Abel, T. 2008, in *AIP Conference Proceedings*, Vol. 990, American Institute of Physics, xiii–xxiii
- O’Shea, B. W., Bryan, G., Bordner, J., et al. 2005, in *Adaptive mesh refinement-theory and applications* (Springer), 341–349
- Ripamonti, E., & Abel, T. 2004, *Monthly Notices of the Royal Astronomical Society*, 348, 1019
- Sanati, M., Revaz, Y., Schober, J., Kunze, K. E., & Jablonka, P. 2020, *Astronomy & Astrophysics*, 643, A54
- Schmidt, W., Federrath, C., Hupp, M., Kern, S., & Niemeyer, J. C. 2009, *Astronomy & Astrophysics*, 494, 127
- Shu, C.-W., & Osher, S. 1988, *Journal of computational physics*, 77, 439
- Tegmark, M., Silk, J., Rees, M. J., et al. 1997, *The Astrophysical Journal*, 474, 1
- Toro, E. F. 2013, *Riemann solvers and numerical methods for fluid dynamics: a practical introduction* (Springer Science & Business Media)
- Tseliakhovich, D., & Hirata, C. 2010, *Physical Review D*, 82, 083520
- Turk, M. J., Abel, T., & O’Shea, B. 2009, *Science*, 325, 601
- Turk, M. J., Clark, P., Glover, S. C., et al. 2010, *The Astrophysical Journal*, 726, 55
- Umeda, H., & Nomoto, K. 2005, *The Astrophysical Journal*, 619, 427
- Van Leer, B. 1979, *Journal of computational Physics*, 32, 101
- Wagstaff, J. M., Banerjee, R., Schleicher, D., & Sigl, G. 2014, *Physical Review D*, 89, 103001
- Wang, P., Abel, T., & Zhang, W. 2008, *The Astrophysical Journal Supplement Series*, 176, 467
- Wise, J. H., & Abel, T. 2008, *ApJ*, 685, 40
- Wise, J. H., Turk, M. J., & Abel, T. 2008, *The Astrophysical Journal*, 682, 745
- Yoshida, N. 2019, *Proceedings of the Japan Academy, Series B*, 95, 17
- Yoshida, N., Abel, T., Hernquist, L., & Sugiyama, N. 2003, *The Astrophysical Journal*, 592, 645
- Yoshida, N., Bromm, V., & Hernquist, L. 2004, *The Astrophysical Journal*, 605, 579
- Yoshida, N., Omukai, K., & Hernquist, L. 2008, *Science*, 321, 669
- Yoshida, N., Omukai, K., Hernquist, L., & Abel, T. 2006, *The Astrophysical Journal*, 652, 6